crystals

MDPI

Article

Synthesis, Crystallographic Structure, Stability, and HSA-Binding Affinity of a Novel Copper(II) Complex with Pyridoxal-Semicarbazone Ligand

Violeta Jevtovic [1], Aleksandra Rakić [2], Jelena M. Živković [3], Aljazi Abdullah Alrashidi [1], Maha Awjan Alreshidi [1], Elham A. Alzahrani [1], Odeh A. O. Alshammari [1], Sahar Y. Rajeh [1], Mostafa A. Hussien [4] and Dušan Dimić [2,*]

[1] Chemistry Department, College of Science, University of Ha'il, Ha'il 81451, Saudi Arabia
[2] Faculty of Physical Chemistry, University of Belgrade, Studentski Trg 12-16, 11000 Belgrade, Serbia
[3] Innovative Centre of Faculty of Chemistry, Studentski Trg 12-16, 11000 Belgrade, Serbia
[4] Department of Chemistry, Faculty of Science, King Abdulaziz University, Jeddah 21589, Saudi Arabia
* Correspondence: ddimic@ffh.bg.ac.rs

Abstract: Copper–semicarbazone ligands have been extensively investigated for several medicinal applications. In this contribution, a novel copper(II) complex with a pyridoxal–semicarbazone ligand, [Cu(PLSC)Cl(H_2O)](NO_3)(H_2O), was synthesized and characterized by X-ray crystallography, elemental analysis, UV-VIS, and FTIR spectroscopies. The stabilization interactions within the structure were assessed using the Hirshfeld surface analysis. The crystallographic structure was optimized at the B3LYP/6-311++G(d,p)(H,C,N,O)/LanL2DZ(Cu) level of theory. A comparison between the experimental and theoretical bond lengths and angles was undertaken to verify the applicability of the selected level of theory. The obtained high correlation coefficients and low mean absolute errors confirmed that the optimized structure is suitable for further investigating the interactions between donor atoms and copper, along with the interactions between species in a neutral complex, using the Quantum Theory of Atoms in Molecules approach. The electrostatic potential surface map was used to reveal distinct charge distributions. The experimental and calculated FTIR spectra were compared, and the most prominent bands were assigned. The interactions with human serum albumin (HSA) were assessed by spectrofluorometric titration. The spontaneity of the process was proven, and the thermodynamic parameters of binding were calculated. Molecular docking analysis identified the most probable binding site, providing additional insight into the nature of the interactions.

Keywords: copper(II) complex; DFT; QTAIM; HSA; Hirshfeld surface analysis

check for updates

Citation: Jevtovic, V.; Rakić, A.; Živković, J.M.; Alrashidi, A.A.; Alreshidi, M.A.; Alzahrani, E.A.; Alshammari, O.A.O.; Rajeh, S.Y.; Hussien, M.A.; Dimić, D. Synthesis, Crystallographic Structure, Stability, and HSA-Binding Affinity of a Novel Copper(II) Complex with Pyridoxal-Semicarbazone Ligand. *Crystals* **2024**, *14*, 1106. https://doi.org/10.3390/cryst14121106

Academic Editor: Kil Sik Min

Received: 12 December 2024
Revised: 19 December 2024
Accepted: 20 December 2024
Published: 23 December 2024

Copyright: © 2024 by the authors. Licensee MDPI, Basel, Switzerland. This article is an open access article distributed under the terms and conditions of the Creative Commons Attribution (CC BY) license (https://creativecommons.org/licenses/by/4.0/).

1. Introduction

The semicarbazide derivatives of the type R–CH=N–NH–CX–NH_2, often named semicarbazones, are obtained in the reaction between semicarbazides and aldehydes/ketones [1]. Depending on the aldehyde/ketone, these compounds behave as unidentate, bidentate, or multidentate chelating agents [2]. The increased stability, chelating properties, and structural versatility of these ligands have led to the preparation of many transition metal compounds [3,4]. The formed complexes are vividly colored, and the complexation procedure was suggested for the analytical determination of selected metal ions [5]. As their mechanism of action greatly depends on the present substituents, the fine-tuning of activity is possible through structural description and analysis [1]. Also, several protonation/deprotonation sites lead to the neutral, monoanionic, and dianionic forms (Figure 1) [6]. More details on the structural features and applications of semicarbazone-derived metal complexes can be found in reference [7].

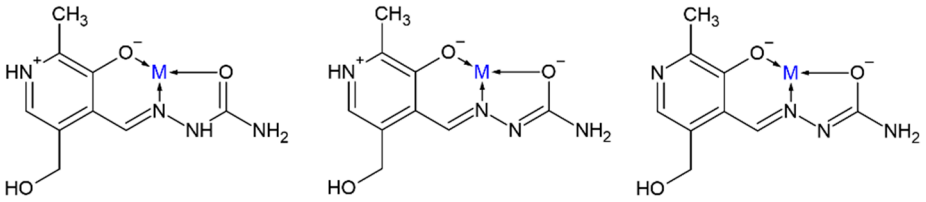


Figure 1. Different binding modes of PLSC ligand.

Copper semicarbazone complexes have been extensively examined for several medicinal applications as anticancer reagents, radical scavengers, and positron emission tomography (PET) agents for imaging [8]. In the paper by Muleta and Desalegn, the synthesis and structural characterization of heteroleptic copper(II) complexes of natural product-based semicarbazone ligands were described, and they showed higher antibacterial activity on *Streptococcus pyogenes* bacteria than the respective ligands [9]. The study of Chau and coworkers proved that lipophilic anions increase the cytotoxicity of cationic copper(II) semicarbazone compounds [10]. Estradiol-based salicylaldehyde thiosemicarbazone complexes with copper(II) showed cytotoxicity toward MCF-7, MCF-7 KCR, DU-145, and A549 cancer cells along with antibacterial activity toward Staphylococcus aureus bacteria strain [11]. Electron paramagnetic resonance spectroscopy (EPR) is particularly useful for the determination of the oxidation state of copper and the geometry of its complexes, as explained in [12].

Theoretical methods are important for examining the stabilization and structural properties of copper(II) complexes. The optimization of the structure with the help of Density Functional Theory (DFT) methods allows the determination of structural parameters, the effects of substituents, charges, electron transitions, and reactivity [13,14]. Salbego and coworkers used the QTAIM approach to study the stability of pentacoordinated copper(II)–semicarbazone complexes in relation to hexacoordinated complexes [15]. The Hirshfeld surface analysis of copper(II) semicarbazone complexes allows the determination of different contributions of specific interactions to the overall stability [16,17]. The molecular docking simulations were applied to examine the molecular aspects of interactions with proteins and DNA in references [18,19].

Pyridoxal–semicarbazone (PLSC) is a tridentate ligand obtained from pyridoxal and semicarbazone [20,21]. It contains three donating atoms: phenolic oxygen, azomethine nitrogen, and carbonyl oxygen. The neutral form of the PLSC ligand is protonated at the pyridine nitrogen and azomethine nitrogen sites. Several copper(II) complexes with PLSC are known in the literature, such as $[Cu(PLSC)Br_2]$ [22], $[\{Cu(\mu\text{-}PLTSC)(H_2O)\}_2](SO_4)_2 \cdot 6H_2O$ (**2**) and $[\{Cu(\mu\text{-}PLTSC)(H_2O)\}_2](SO_4)_2 \cdot 2H_2O$ [23], and $[Cu(PLSC)(H_2O)(SO_4)]_2 \cdot 3H_2O$ [24]. As the starting compounds for the synthesis of the title complex include copper(II) chloride and PLSC, it is important to mention that other similar complexes such as $[Cu(PLSC)Cl_2]$ [24,25] have been extensively examined. Complexes of PLSC with nickel, zinc, and other metal complexes are described in [26,27].

The aim of this contribution is to present a comprehensive study of the structural and stability properties of a novel copper(II) complex with PLSC ligand, $[Cu(PLSC)Cl(H_2O)](NO_3)(H_2O)$. The experimental structure was determined by X-ray diffraction analysis and optimized at the B3LYP/6-311++G(d,p)(H,C,N,O)/LanL2DZ(Cu) level of theory. The structural parameters were compared to verify the applicability of the applied level of theory. The Hirshfeld surface analysis examined the intermolecular interactions within the crystallographic structure, emphasizing the interactions between the complex cation, nitrate anion, and co-crystalized solvent molecule. The Quantum Theory of Atoms in Molecules (QTAIM) analysis was used to assess the stability of the structure together with intramolecular interactions between the donor atoms and the central metal ion. The experimental and theoretical vibrational spectra were compared to discuss the applied theory level. The interactions between a complex and a major transport protein, human serum albumin (HSA),

were investigated by spectrofluorometric titration and molecular docking simulations. The most probable interaction site for the mentioned process was described.

2. Materials and Methods

2.1. Chemicals

The solvents used, copper(II)-chloride, nitric acid, human serum albumin, sodium phosphate dibasic, potassium phosphate monobasic, sodium chloride, and potassium chloride, were obtained from Merck (Darmstadt, Germany) and used without further purification.

2.2. Synthesis of PLSC Ligand

The PLSC ligand was obtained as explained in reference [6]. The structural characterization of the ligand included FTIR spectra and elemental analysis. Anal. Calcd. for PLSC·2H_2O ($C_9H_{16}N_4O_5$, 260.25): C, 41.53; H, 6.19; N, 20.52. Found: C, 42.02; H, 6.28; N, 20.52. FTIR: 3461 (υ(O–H) stretching), 1570 (υ(C=N)), 1500 (υ(C–N)), 2956 cm^{-1} (υ($^+$NH)); broad band above 3000 cm^{-1} was assigned to the hydrogen bonded groups. These spectral characteristics closely match those in the mentioned reference.

2.3. Synthesis of [Cu(PLSC)Cl(H_2O)](NO_3)(H_2O)

An amount of 0.1 mmol PLSC ligand was dissolved in water with stirring at high temperature, practically until boiling. Then, 0.1 mmol of $CuCl_2$ was added to the aqueous solution of the mostly dissolved ligand. The addition of salt resulted in an intense green coloring of the solution. However, fragments of the undissolved ligand remained, and therefore, a diluted HNO_3 solution was added (final concentration of HNO_3 was 1×10^{-5} M) to lower the pH, and the ligand and added salt were completely dissolved. The clear, green-colored solution was put at room temperature to crystallize. After 24 h, green single crystals were separated. Yield: 0.24 g (74%). Anal. Calcd. for [Cu(PLSC)Cl(H_2O)](NO_3)(H_2O) ($C_9H_{16}ClCuN_5O_8$, 421.27): C, 25.66; H, 3.80; N, 16.63. Found: C, 25.36; H, 4.10; N, 16.72.

2.4. Characterization

The experimental vibrational spectra were obtained on a Thermo Nicolet-Avatar 370 FTIR spectrometer (Thermo Fisher Scientific, Waltham, MA, USA) between 4000 and 600 cm^{-1}. Around 2 mg of the sample was mixed with 150 mg of potassium bromide, and a pellet was prepared. The electronic spectra of the complex were recorded on a Thermo Scientific UV-VIS Spectrometer (Thermo Fisher Scientific, Waltham, MA, USA) between 800 and 250 nm. The resolution was set to 1 nm with an integration time of 0.20 s. The stock solution in DMF was prepared (final concentration 7×10^{-3} M) and further diluted in water to 5×10^{-3} M. The elemental composition was determined on an Elementar Vario El III (Elementar Analysesysteme GmbH, Langenselbold, Germany) by calculating the mass percentages of different oxides. The molar conductivity measurements were performed on WTW inoLab Cond 720 Conductometer (Thermo Fisher Scientific, Waltham, MA, USA) for 10^{-3} M solution in DMF.

2.5. X-Ray Crystallographic Analysis

A green prismatic crystal (0.218 × 0.133 × 0.115 mm) was taken and installed on a nylon cryoloop. The experimental data were obtained at 123 K by utilizing CuK_λ radiation (λ = 1.54184 Å) on a Rigaku Synergy S diffractometer fitted with a HYPIX 6000 hybrid photon counting detector. Data were collected and corrected by empirical (multi-scan) absorption correction in CrysAlisPro software [28]. The structure was solved and refined by the SHELX software suite and the Olex2 graphical interface [29,30]. The positions of non-hydrogen hydrogen atoms attached to carbon were determined as previously explained [6]. The positions of hydrogen atoms attached to oxygen and nitrogen were determined in the difference Fourier map and were refined with restrained geometry (DFIX/DANG); d(N–H) = 0.91(2) or d(O–H) = 0.88(2) Å.

The obtained crystallographic data were included in the Cambridge Crystallographic Data Centre (CCDC, 12 Union Road, Cambridge CB2 IEZ, UK; e-mail depos-it@ccdc.cam.ac.uk) with the CCDC number 2348548. Important parameters for the structure refinement are presented in the following table.

2.6. Hirshfeld Surface Analysis

The intermolecular interactions within the crystallographic structure are important for explaining its properties. In this contribution, the CrystalExplorer program [31] was used for the Hirshfeld surface analysis, as described previously for similar compounds [6]. The interactions were examined through a graphical representation of two distances, the first one being between two nearest nuclei (d_e) and the other connecting nuclei with the external surface (d_i) [32,33]. These points were colored by comparing the van der Waals separation between nuclei. The normalized distances were between −0.7021 (red) and 1.0586 (blue). The percentages of specific interactions are presented in figures within the Supplementary Materials.

2.7. Quantum Chemical Analysis

The structure optimization was performed in the Gaussian 09 program package (Gaussian 09, revision C 01) [34] starting from the experimental structure. The functional selected for the optimization was B3LYP [35] together with 6-311++G(d,p) basis set [36] for H, C, N, and O atoms and LanL2DZ [37,38] for copper ions. The structures of complex cation, neutral complex, and complex with one water molecule were optimized by following the same procedure. The stabilization interactions between the central metal ion and donor atoms and weak interactions between species were investigated by the Quantum Theory of Atoms in Molecules (QTAIM), as proposed by Bader [39,40]. Several parameters, among them electron density and Laplacian at Bond Critical Points (BCPs), were obtained and are discussed in the main text. The AIMAll program package [41] was employed starting from .wfx files from the Gaussian 09. The electrostatic potentials for metal complex, nitrate ion, and water molecule were separately computed at M06L-GD3/def2-TZVPP level on surfaces defined as the 0.001 a.u. (electronbohr^{-3}) contours of the electronic densities, as suggested by Bader et al. [42]

2.8. Spectrofluorimetric Determination of HSA Binding Affinity

The affinity of the complex toward HSA was monitored by the spectrofluorometric titration on a Cary Eclipse MY2048CH03 spectrophotometer (Agilent Technologies, Santa Clara, CA, USA). The slits were 5 nm, and the scan rate was 600 nm min^{-1}. The final concentration of HSA in the phosphate buffer saline (pH = 7.4, concentrations of NaCl and KCl were 137 and 2.7 mM, respectively) was 5×10^{-6} M. The excitation wavelength was 295 nm, and this energy was sufficient for the excitation of tryptophan residues in the protein structure. The concentration of the complex changed between 1 and 10×10^{-6} M. The interactions were followed by a decrease in the intensity of emission maxima, as quantified by the double-log Stern–Volmer equation [43]:

$$\log\left(\frac{F_0 - F}{F}\right) = \log K_b + n\log[complex] \quad (1)$$

In the presented equation, F_0 and F are the fluorescence emission intensities of HSA solution without and with the added complex, K_b is the binding constant, and n is the number of binding positions. The changes in enthalpy and entropy of binding were calculated from the Van 't Hoff's plot, which included binding constants determined at three temperatures (27, 32, and 37 °C):

$$\ln K_b = -\frac{\Delta H_b}{RT} + \frac{\Delta S_b}{R} \quad (2)$$

2.9. Molecular Docking

The material for molecular docking calculations was sourced from the Protein Data Bank. A newly synthesized and crystallographically characterized Cu(II) complex with PLSC, aqua, and chlorido ligands was utilized as the docking molecule. These calculations were designed to support and rationalize experimental findings at the molecular level, using HSA as the target protein. The 2BXN structure [44] was specifically selected due to naturally occurring myristic acids bound to the structure of HSA, allowing for a closer approximation of physiological conditions in the human body.

Target preparation involved cleaning the 2BXN structure of all ligands and water molecules, retaining only myristic acid, resulting in the modified structure termed HSA-myristate. This preparation was deemed appropriate for approximating physiological conditions. The XYZ coordinates of the $[Cu(PLSC)Cl(H_2O)]^+$ crystal structure were optimized using Gaussian 09 at the B3LYP/6-311++G(d,p)(H,C,N,O)/LanL2DZ(Cu) level of theory, as previously explained.

Molecular docking calculations were conducted using AutoDock 4.2.6 integrated within the AMDock program [45] (version 1.5.2), under conditions of ambient temperature (25 °C) and physiological pH (7.4). Visualization and analysis of interactions and binding to 2BXN-myristate were performed using Biovia Discovery Studio Visualizer v21.1.0.20298.

3. Results and Discussion

3.1. Crystallographic Structural Analysis

The compound $[Cu(PLSC)Cl(H_2O)](NO_3)(H_2O)$ was prepared from the mixture of PLSC solution, copper(II) chloride, and nitric acid, which was added to increase the solubility of the ligand. The experimental structure of the title compound is depicted in Figure 2a. This structure consists of a PLSC ligand in neutral form with an ONN donor system, chlorido ligand, and aqua ligand directly attached to the central metal ion. Additionally, a nitrate anion is present in the outer sphere of the complex, leading to the neutrality of the obtained species. A water molecule that is bound to protonated pyridine nitrogen is also present. The PLSC ligand is in neutral form, as the structure contains protonated pyridine nitrogen, deprotonated phenyl oxygen, and protonated azomethine nitrogen, similar to the nickel(II) complex with the same ligand [6]. Experimental bond lengths and angles are presented in Tables S1 and S2. The distances between the copper(II) and oxygen atoms are 1.8986(14) (O1) and 1.9699(14) Å (O3). The presence of phenyl attached to an oxygen atom in position 1 leads to a lower bond length. The bond between Cu(II) and azomethine nitrogen has a length of 1.9860(16) Å. Even longer distances are found between the copper(II) ion and aqua (2.3439(15) Å)/chlorido (2.2750(5) Å) ligands. These values correspond well to the donating abilities of the donor atoms, although some are influenced by the presence of other interactions, as in the case of the aqua ligand. The overall geometry is octahedral, but it can be assumed that the water molecule and nitrate anion influence the stability of the structure. The angle between the oxygen atoms and Cu(II) is 169.91(6)°, which deviates from linearity because of the rigidity of the PLSC ligand. The same applies to the angle denoted as O3–Cu–N2, which has a value of 80.71(6)°. There is also an incline of the aqua ligand toward the nitrate anion, which leads to O1–Cu–O4 and N2–Cu–O4 angles higher than 96°.

According to Table 1, the title complex crystallizes in a triclinic *P-1* space group. Within the crystallographic structure, there are several hydrogen bonds formed. These interactions are shown in Table 2. Within one unit, the hydrogen bond exists between the aqua ligand and nitrate anion, with a bond distance of 1.97(2) Å and an angle of 154(3)°. Previously, interactions between aqua ligands and a sulfate anion coordinated to a nickel(II) central metal ion were shown in reference [6]. The second hydrogen bond is formed between protonated pyridine nitrogen and a solvent molecule. The distance between the hydrogen and oxygen atoms is lower (1.827(18) Å) due to the electronegativity of the groups. The crystallographic structure includes an infinite linear chain in which cations are connected through interactions between the water molecule in the outer sphere of one unit and

the hydroxymethyl group of the second unit (Figure 2, denoted as O(8)–H(8E)· · · O(7) in Table 2) with a bond distance of 2.03(2) Å. Additionally, interactions between the ending amino group and oxygen atom in position 3 stabilize the structure. These hydrogen bonds have a length of around 2.03 Å. The 3-D structure of the obtained compound presents a 3-D hydrogen-bonded network of parallel stacked 2-D sheets (Figure 2). This structure is supported by the existence of a Cu–OH_2 bond. The aqua ligand interacts with the nitrate anion of the second unit (1.91(2) Å), while the oxygen atom of the hydroxymethyl group forms a hydrogen bond with the chlorido ligand (2.24(2) Å).

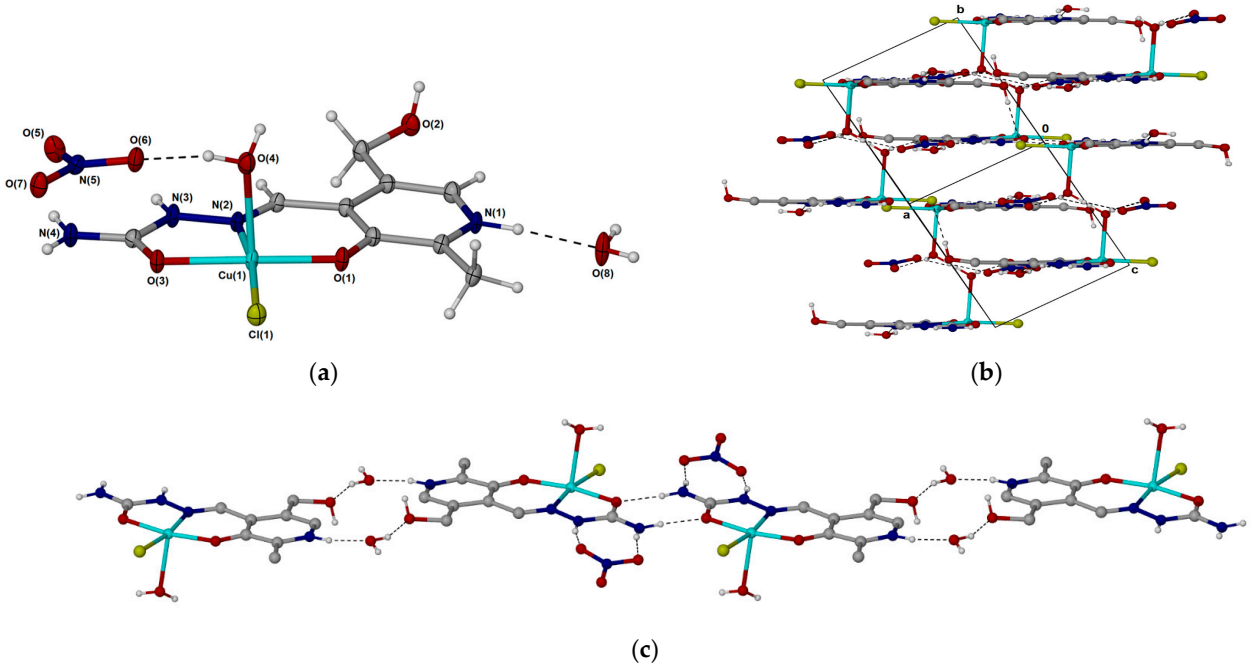


Figure 2. (**a**) Molecular diagram of [Cu(PLSC)Cl(H_2O)][NO_3]·H_2O with non-hydrogen atoms represented by 50% displacement ellipsoids and hydrogen atoms as spheres of arbitrary size. (**b**) The overall structure is a 3-D hydrogen bonded network, comprised of parallel stacked 2-D sheets, supported by the Cu–OH_2 bond. (**c**) The structure is composed of infinite linear chains of [Cu(L)Cl(H_2O)]$^+$ cations with N–H· · · O and O–H· · · O hydrogen bonds to the [NO_3]$^-$ anions and water molecules. Further hydrogen bonding through the [NO_3]$^-$ anion and the water molecules connects the chains into a 2-D sheet.

Table 1. Crystal data of the newly obtained complex.

Empirical Formula	**[Cu(PLSC)Cl(H_2O)](NO_3)(H_2O) $C_9H_{16}ClCuN_5O_8$**
Formula weight	421.26
Temperature (K)	123(2)
Crystal system	Triclinic
Space group	P-1
Radiation/wavelength [Å]	1.54184
Volume (Å^3)	793.68(3)
Unit cell dimension (Å/°)	a = 6.9247(2) b = 8.0762(2) c = 13.9679(3) α = 96.478(2) β = 104.111(2) γ = 93.411(2)
Z	2

Table 1. *Cont.*

Empirical Formula	**[Cu(PLSC)Cl(H_2O)](NO_3)(H_2O) $C_9H_{16}ClCuN_5O_8$**
Calculated density (Mg m^{-3})	1.8666
Goodness-of-fit on F^2	1.114
h, k, l_{max}	8, 10, 17
N_{ref}	3208
Bond precision: C–C (Å)	0.003
Data completeness	0.985
Θ max [°]	79.819
R1 [$I > 2s(I)$], R1 (*all*)	0.0320
*w*R2 [$I > 2s(I)$], *w*R2 (*all*)	0.0910
CCDC no.	2348548

Table 2. Hydrogen bonds for [Cu(PLSC)Cl(H_2O)](NO_3)(H_2O) [Å and °].

D-H···A	**d(D-H)**	**d(H···A)**	**d(D···A)**	**<(DHA)**
O(2)–H(2)···Cl(1)#1	0.847(18)	2.24(2)	3.0816(16)	170(4)
O(4)–H(4A)···O(6)	0.846(18)	1.97(2)	2.758(2)	154(3)
O(4)–H(4B)···O(5)#2	0.854(17)	1.91(2)	2.716(2)	158(3)
O(8)–H(8E)···O(7)#3	0.835(17)	2.03(2)	2.826(2)	160(3)
O(8)–H(8D)···O(2)#4	0.842(18)	2.12(2)	2.890(2)	153(3)
N(1)–H(1N)···O(8)	0.883(17)	1.827(18)	2.703(2)	171(3)
N(3)–H(3N)···O(6)#5	0.876(17)	2.052(19)	2.906(2)	165(3)
N(4)–H(4N)···O(7)#5	0.884(18)	2.010(18)	2.886(2)	171(3)
N(4)–H(5N)···O(3)#6	0.874(18)	2.036(18)	2.903(2)	171(3)

Symmetry transformations used to generate equivalent atoms: #1 $x + 1, y + 1, z$; #2 $-x, -y + 1, -z$; #3 $x + 1, y + 1, z + 1$; #4 $-x + 2, -y + 2, -z + 1$; #5 $x + 1, y, z$; #6 $-x, -y, -z$.

3.2. UV-VIS Spectral Analysis

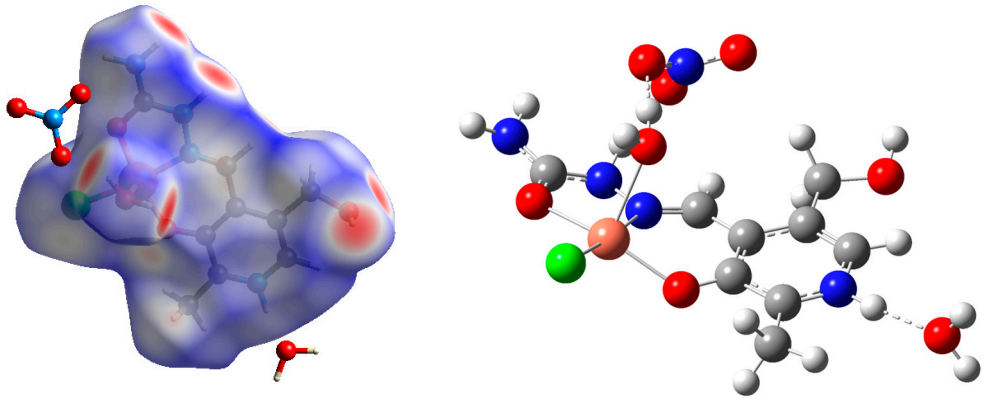
The UV-VIS spectrum of the title complex was recorded in aqueous solution at a final concentration of 5×10^{-4} M. Prior to this, a stock solution of the complex was prepared in DMF. The experimental UV-VIS spectrum between 800 and 250 nm is shown in the Supplementary Materials as Figure S1. As can be seen, there are two broad peaks at 398 and 298 nm, similar to other complexes with PLSC ligands [6,46]. The peak at 298 nm originates from the ligand, including n→π* transitions associated with the imine group and the pyridine ring. The same transition was observed in the spectrum of the free ligand [47]. The second peak can be assigned to the ligand-to-metal charge transfer (LMCT) transition between the central metal ion and azomethine nitrogen. The charge transfer between the chlorido ligand and copper(II) ion is expected around 330 nm, and it can be assumed that this band is overlapped with other more intense bands in the spectrum [48]. The transitions within the electronic structure of copper(II), marked as d→d, were not observed in the spectrum. This absence is likely due to their low intensity and overlap with the CT band. A similar result was found in previous research [6].

3.3. Molar Conductivity Measurements

The obtained complex was soluble in DMF, and the molar conductivity measurements were performed for a 10^{-3} M solution. The obtained value of 88 S cm^2 mol^{-1} indicates a 1:1 type electrolyte [49]. This result proves the assumption that the chlorido ligand is coordinated directly with the central metal ion in the solution. Similar values were obtained for other copper(II) complexes with similar ligands [23]. The exchange of chlorido ligands was observed in the case of [Cu(PLSC)Cl_2], which acted as a 1:2 type electrolyte in the solution [24].

3.4. Hirshfeld Surface Analysis

Stabilizing interactions are fundamental to experimental structures, governing the distribution of their components. Hirshfeld surface analysis was employed to identify and quantify these interactions. Notably, the Hirshfeld surface of the square-pyramidal copper(II) complex excludes both the nitrate ion and the free water molecule present in the second coordination sphere of the complex (Figure 3). The fingerprint plots of the selected interactions are given as the Supplementary Materials.



(**a**) (**b**)

Figure 3. (**a**) Hirschfeld surface (normalized distances between −0.7021 (**red**) and 1.0586 (**blue**)) and (**b**) optimized structure (at B3LYP/6-311++G(d,p)(H,C,N,O)/LanL2DZ(Cu) level of theory) of [Cu(PLSC)Cl(H_2O)](NO_3)(H_2O).

The most prominent interactions in the experimental structure are found between the oxygen and hydrogen atoms (O···H), accounting for 32.4% of all contacts. The presence of a water molecule coordinated with the central metal ion significantly increases the strength of the hydrogen bond interaction with molecules from the environment [50]. Additionally, oxygen atoms present in the aqua ligand and hydroxymethyl group serve as donors of hydrogens in the mentioned interactions. Another notable type of contact is H···H, accounting for 28.2% of the total interactions. The large number of hydrogen atoms in the structure plays an important role in stabilizing the compound through these interactions. Furthermore, Cl···H interactions are also observed, contributing 9.9% to the total contacts.

Protonated pyridine, protonated azomethine nitrogen, and amino nitrogen atoms are part of the N···H contacts (3.5%). The hydrogen bonds involving the amino group gain strength upon coordination, further stabilizing the structure [51]. Carbon–hydrogen interactions amount to 6.6%. Interactions involving electronegative atoms occur at relatively low frequencies, with O···O and O···N contacts contributing just 0.9% and 0.2%, respectively. Similarly, interactions involving carbon and oxygen or nitrogen atoms account for 1.9% (C···O) and 0.7% (C···N) of the total contacts, respectively. The central metal ion is included in 1.2% of the interactions.

3.5. Theoretical Structural Analysis and QTAIM

The theoretical structure was obtained at the B3LYP/6-311++G(d,p)(H,C,N,O)/LanL2DZ(Cu) level of theory. This level of theory was chosen as it was previously shown that it can be used to predict the spectra and reactivity of complexes with similar ligands. Its applicability is proven by comparing the structural parameters through the calculation of the parameters (coefficient and mean absolute error (MAE)), as discussed previously [6]. It is important to mention that structures of the complex cation ([Cu(PLSC)Cl(H_2O)]$^+$) and neutral species with the water molecule in the outer sphere ([Cu(PLSC)Cl(H_2O)](NO_3)(H_2O)) were selected to examine the structural differences upon binding of the anion and solvent molecule. The optimized structure of the neutral species is presented in Figure 3, while the

structural parameters (bond lengths and angles) are listed in the Supplementary Materials (Tables S1 and S2).

The bond lengths between oxygen atoms of PLSC and copper(II) were 1.8986(14) and 1.9699(14) Å, respectively, in the crystallographic structure and 1.987 and 2.089 Å, respectively, in the optimized structure. Once the solvent molecule and anion were removed, the bond distances were lowered to 1.968 and 2.075 Å. On the other hand, the Cu–N bond distance was 1.9860(16) in the experimental and 2.041/2.072 Å in the theoretical structures. These results prove that the mentioned interactions were not significantly influenced by the presence of the anion and solvent molecule due to the rigidity of the PLSC ligand and extended delocalization throughout its structure. The bond distances between the central metal ion and chlorido/aqua ligands were also well reproduced. The correlation coefficient and MAE in the case of the neutral complex were 0.995 and 0.023 Å, respectively. Once the anion and water molecule were removed, these parameters were 0.996 and 0.025 Å. It should be outlined that the differences between the experimental and theoretical bond lengths were much lower (0.012 Å) when interactions involving copper(II) were removed. This was expected due to the rigidity of PLSC and the interchanging single and double bonds.

The bond angles are more susceptible to the change in the presence of the water molecule and nitrate anion. The correlation coefficient and MAE values in the case of bond angles for the optimized structure of the complex were 0.984 and 2.15°, respectively. When the structure of the complex cation was compared with the crystallographic structure, these parameters were 0.989 and 1.80°. These differences result from the slight incline of the aqua ligand toward the nitrate anion, as explained in the first section. The difference between the experimental and theoretical bond angle values was found for N2–Cu–O4. The experimental value was 88.45(6)°, while the theoretical values were 82.57 (neutral structure) and 85.92° (complex cation). This is a direct consequence of the interaction between the aqua ligand and nitrate anion. The structure of the neutral complex is probably changed in the solution. Therefore, the structure of the complex cation is more important for molecular docking studies. The angle of O1–Cu–O3 was significantly changed, from 169.91(6) to 157.40/161.19°, due to the system's relaxation, as the optimization was performed on an isolated compound. The differences in the other values are much less pronounced. When angles enclosed by atoms of PLSC ligand were selected, the MAE values were much lower (1.30 and 0.96°). Based on these comparisons, it could be concluded that the theoretical structure represented the experimental one well and that the selected level of theory was appropriate for the examined system.

The interactions within the theoretical structure were further examined using the QTAIM approach to the optimized structure. This methodology is suitable for accessing the coordination environment and energy of metal–ligand interactions [52,53]. Interactions between donor atoms and copper(II), along with the weak interactions between species, were quantified through parameters of Bond Critical Points (BCPs), such as electron density ($\rho(r)$), Laplacian ($\nabla^2(r)$), Lagrangian kinetic electron energy ($G(r)$), potential electron energy ($V(r)$), density of total electron energy ($H(r) = G(r) + V(r)$), and interatomic bond energy ($E_{bond} = V(r)/2$) [54]. These values are given in Table 3, while the BCPs are shown in Figure 4.

Selected interactions from Table 3 are characterized by electron density values lower than 0.01 a.u. and positive Laplacians. According to the classification proposed by Bader and Essen, interactions can be divided into two groups. The first includes shared interactions (covalent bonds) with a high electron density, while the second one contains closed-shell interactions with an electron density lower than 0.01 a.u. Interactions such as ionic bonds, van der Waals interactions, and hydrogen bonds belong to the second group [55,56]. As can be seen in Table 3, interactions between copper(II) and surrounding atoms have electron densities between 0.031 (Cu–OH_2) and 0.072 a.u. (Cu–N2). These values depend highly on the optimized bond length and the surrounding groups in the PLSC structure. A more detailed classification was proposed by Bianchi and coworkers.

They divided interactions based on the relative ratio of G(r) and V(r). The covalent bonds have values of –G(r)/V(r) lower than 1, the intermediate (transit) region is characterized by the value of this parameter between 1 and 2, while ionic bonds and van der Waals interactions have values higher than 2 [57]. All of the mentioned interactions with copper(II) are close to the intermediate region when –G(r)/V(r) is concerned. The interaction with chlorine has a higher covalent character, while those with oxygen and nitrogen are within the transient region between covalent and ionic bonds. Additional proof for the covalent character of the Cu–Cl and Cu–N bond is the negative value of the density of the total energy of electrons (H(r)) [54]. Similar characteristics of Cu–N bonds were observed for other pentacoordinated copper(II)-semicarbazone complexes [15]. This value is higher than zero for the other four interactions, indicating a partial ionic character. The interatomic bond energies also greatly depend on the distance and surrounding groups. The interaction energy value was calculated using the Espinosa approach [58]. The strongest interactions were between Cu(II) and phenolic oxygen/azomethine nitrogen ($-153.4/-147.2$ kJ mol^{-1}). This is expected, as both atoms are attached to the groups with extended delocalization, leading to the possibility of donation. The interaction with the aqua ligand is classified as the weakest (-40.2 kJ mol^{-1}).

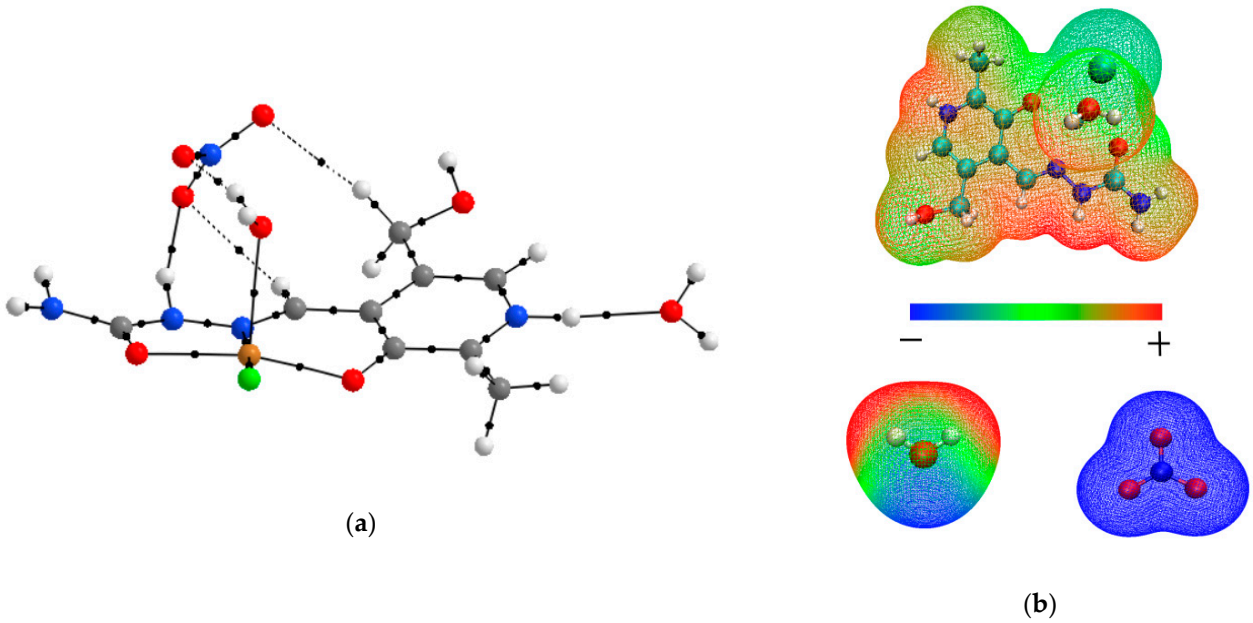
Table 3. The selected Bond Critical Point (BCP) of the obtained complex.

Bond	ρ(r) [a.u.]	$\nabla^2\rho(r)$ [a.u.]	G(r) [kJ mol^{-1}]	V(r) [kJ mol^{-1}]	H(r) [kJ mol^{-1}]	−G(r)/V(r)	E_{bond} [kJ mol^{-1}]
Cu–O1	0.071	0.497	316.3	−306.7	9.6	1.0	−153.4
Cu–O3	0.056	0.374	226.7	−208.2	18.6	1.1	−104.1
Cu–N2	0.072	0.421	285.5	−294.4	−8.9	1.0	−147.2
Cu–Cl	0.069	0.268	193.6	−211.2	−17.6	0.9	−105.6
Cu–OH_2	0.031	0.153	90.4	−80.4	10.0	1.1	−40.2
N–H···OH_2	0.028	0.106	64.5	−59.2	5.3	1.1	−29.6
HO–H···O–NO_2	0.025	0.094	55.5	−49.5	6.0	1.1	−24.7
H_2C–H···O–NO_2	0.010	0.030	17.3	−15.0	2.3	1.2	−7.5
N–H···O–NO_2	0.048	0.133	101.4	−115.4	−14.1	0.9	−57.7
C–H···O–NO_2	0.012	0.039	22.7	−19.9	2.8	1.1	−10.0

There are several other interactions that stabilize the structure of neutral species. The first is formed between protonated pyridine and the co-crystalized solvent molecule as observed in the crystallographic structure. This interaction has a value of electron density of 0.031 a.u., a positive value of H(r) (5.3 kJ mol^{-1}), and a ratio of −G(r) and V(r) higher than 1, which classifies it as a closed-shell interaction with interatomic bond energy of -29.6 kJ mol^{-1}. The importance of the nitrate anion was also proven through QTAIM analysis. Four interactions with this anion were found (Table 3). Among these, the strongest is formed with the ending amino group (-57.7 kJ mol^{-1}). This interaction has a partial covalent character due to the proximity of the groups and the electronegativity of the atoms included. The interaction with the aqua ligand has a value of interatomic bond energy of -24.7 kJ mol^{-1} and is responsible for the change in the relative position of this ligand compared with others. The weakest interactions with the nitrate anion were formed with hydrogen atoms attached to carbon atoms (carbon–hydrogen bonds), with energies of -7.5 and 10.0 kJ mol^{-1}.

The electrostatic potential surface of the crystallographic structure, divided into three components—metal complex, nitrate ion, and free water molecule—reveals distinct charge distributions and offers valuable insights into hydrogen bonding interactions (Figure 4b). For the metal complex, the red regions indicate higher positive potential localized at the hydrogen atoms bonded to electronegative oxygen or nitrogen atoms. The negative

electrostatic potential of the negatively charged nitrate ion is represented by a blue color. At the same time, the neutral water molecule exhibits both regions: blue color (negative electrostatic potential) around its oxygen atom and red color (positive electrostatic potential) around its hydrogen atoms (Figure 4b). Analysis of the crystal structure shows that the positive potential of the hydrogen atom from the coordinated water molecule is directed toward the negative potential of the oxygen atom of the nitrate ion, forming a hydrogen bond (Figures 2b and 4b). Additionally, a hydrogen bond is observed between the positive potential on the hydrogen atom of the N−H group of the pyridine ligand and the negative potential on the oxygen atom of the water molecule.



(**a**) (**b**)

Figure 4. (**a**) BCPs (black circles) connecting atoms within the structure of [Cu(PLSC)Cl(H_2O)](NO_3)(H_2O) and (**b**) electrostatic potential surfaces of the metal complex, nitrate ion, and free water molecule (**a**) and crystal structure (**b**). The potentials were calculated at the M06L-GD3/def2-TZVPP level and mapped at the surfaces defined by an electron density of 0.001 a.u. The atoms in the crystal structure are denoted with the following colors: hydrogen, white; carbon, gray; nitrogen, blue; oxygen, red; chlorine, green; and copper, orange.

3.6. Theoretical and Experimental IR Spectral Analysis

The experimental IR spectrum of the obtained complex was prepared for the solid sample in the KBr pellet. On the other side, the theoretical IR spectrum was calculated for the structure optimized at the B3LYP/6-311++G(d,p)(H,C,N,O)/LanL2DZ(Cu) level of theory. Vibrations were visualized in the GausView program [59]. For this purpose, the optimized structure with anion and solvent molecule in the outer sphere was selected to mimic the experimental conditions. The comparison between the experimental and theoretical spectra is another way to prove the applicability of the chosen level of theory (Figure 5). The correction coefficient was obtained based on the experimental and theoretical wavenumbers (0.982). This parameter accounted for the difference in the physical state of the sample, as the experimental spectrum was recorded for the solid sample, while the theoretical spectrum was predicted for the isolated compound in a vacuum. Some of the most prominent bands in these spectra are mentioned in the following paragraphs.

In the spectral region between 3600 and 2500 cm^{-1}, the most prominent bands are assigned to the X–H (X=C,N,O) stretching vibrations. The band at 3526 cm^{-1} in the theoretical and 3410 cm^{-1} in the experimental spectrum originates from the stretching vibration of the ending amino group of the PLSC ligand. The protonation of pyridine nitrogen leads to a strong peak at 3312 and 3308 cm^{-1} in the theoretical and experimental spectra, respectively. This is an important band for discussing the overall charge of the

PLSC ligand, especially if the crystallographic structure is unavailable. The vibration assigned to the protonated azomethine nitrogen atom is positioned at 2894 cm^{-1}. In the theoretical spectrum, several weak bands between 3700 and 3900 cm^{-1} are assigned to the O–H stretching vibration. These bands in the experimental spectrum form a broad peak centered around 3300 cm^{-1}, showing that these bands are shifted toward lower wavenumbers due to the formation of hydrogen bonds with the neighboring units, as discussed in [60,61]. This shift is expected, as hydrogen-bonding interactions were not included in the theoretical analysis and optimization. The contribution of C–H stretching vibrations is not high, as there are just several positions in which sp^3 and sp^2 carbon atoms are attached to hydrogens. In the theoretical spectrum, these bands are above 3000 cm^{-1} for sp^2 carbon atoms and below 3000 cm^{-1} for sp^3 carbon atoms.

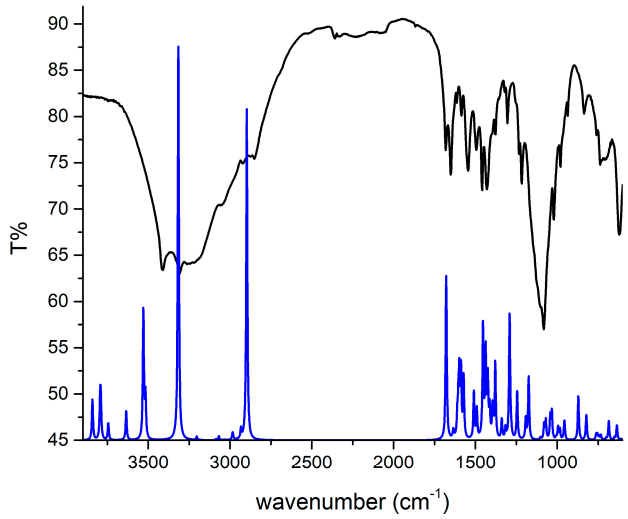


Figure 5. Experimental (black line) and theoretical (at B3LYP/6-311++G(d,p)(H,C,N,O)/LanL2DZ(Cu), blue line) FTIR spectra of $[Cu(PLSC)Cl(H_2O)](NO_3)(H_2O)$.

The second region of the spectrum is located between 2000 and 1000 cm^{-1}. The first medium band is assigned to the C=O vibration of the PLSC at 1678 cm^{-1} in the theoretical and 1683 cm^{-1} in the experimental spectrum. It should be noted that the height of this band is much lower than expected due to the interactions with the central metal ion, although its position matches that in the spectrum of the pure ligand [20]. The C=N stretching vibration is located at 1640 cm^{-1} in the experimental spectrum and 1635 cm^{-1} in the theoretical spectrum. These values are much higher than the wavenumber in the experimental spectrum of the pure PLSC ligand (1570 cm^{-1}) [20]. This is a consequence of the complex formation through Cu–N interaction [6,62]. The asymmetric stretching vibration of the nitrate anion is assigned to the band at 1290 cm^{-1} in the theoretical and 1222 cm^{-1} in the experimental spectrum. It is assumed that part of the intense band between 1100 and 1200 cm^{-1} also includes vibrations of the nitrate anion [63], as it was not observed in the spectra of the other PLSC complexes. This interpretation is supported by the theoretical data. The band around 1100 cm^{-1} belongs to the C–O stretching vibration, as previously shown for the pure ligand and its complexes [64]. The region below 1000 cm^{-1} contains the out-of-plane and torsional vibrations that belong to the backbone structures. The bending vibration of the nitrate anion is positioned at 825 and 820 cm^{-1} in the experimental and theoretical spectra, respectively.

3.7. Experimental and Theoretical Determination of the HSA-Binding Affinity

The interactions between the obtained complex and HSA were determined through spectrofluorometric titration. The excitation of HSA resulted in an emission spectrum with a peak at around 340 nm. A decrease in fluorescence emission intensity was visible upon the addition of the complex, as shown in Figure 6. Notably, additional peaks appeared in

the spectrum at approximately 470 nm, suggesting the presence of an additional fluorescent species in the solution. This phenomenon likely arises from interactions of the complex and protein, altering the chemical environment of the tryptophan residues. The measurements were performed at three temperatures to allow for the calculation of the thermodynamic parameters of binding.

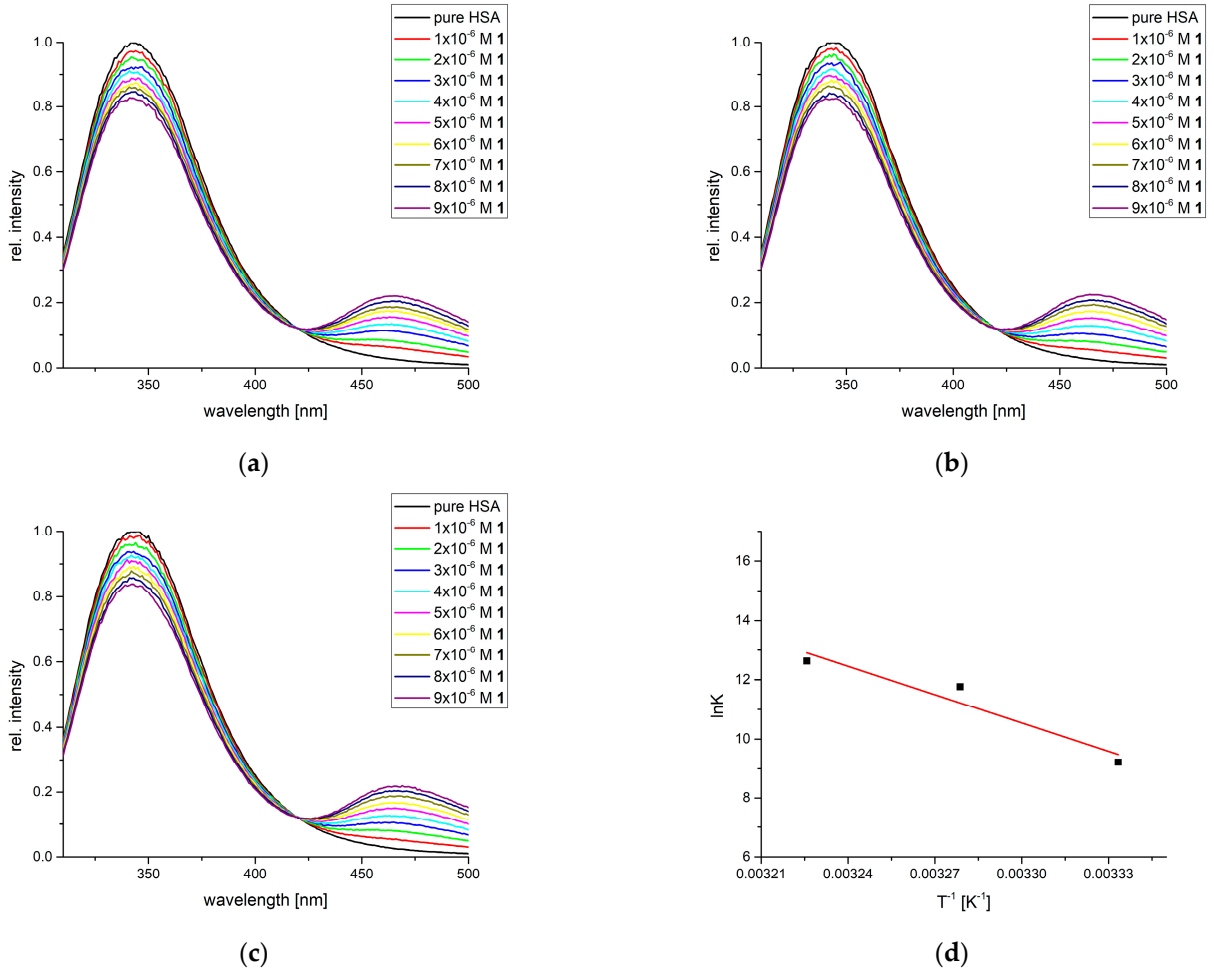


Figure 6. Fluorescence emission spectra of HSA for the titration with various concentrations of [Cu(PLSC)Cl(H_2O)](NO_3) at (**a**) 27°, (**b**) 32°, and (**c**) 37 °C and (**d**) the Van 't Hoff plot for the binding process.

The fluorescence intensity was dependent on the quencher concentration, as predicted by Equation (1). The data describing the binding process are presented in Table 4. The linearity of the plots was verified by the R^2 values higher than 0.99. The number of binding positions was between 0.929 for 27 °C and 1.226 for 37 °C. These values show the interaction between one complex molecule and one HSA molecule. The calculated binding constants were 1.01×10^{-4}, 5.11×10^{-5}, and 5.48×10^{-5} M^{-1} in the temperature range between 27 and 37 °C. These values resemble those obtained for the nickel(II) complex with PLSC ligand [6]. The changes in enthalpy and entropy of the process were 264.1 kJ mol^{-1} and 959.2 J mol^{-1} K^{-1}, respectively. Based on the values of these parameters, the most probable interactions between the complex and protein molecules can be determined. Positive changes in the enthalpy and entropy of the process indicate the formation of non-specific interactions, such as van der Waals and hydrophobic [65]. The spontaneity of the binding process was shown by calculating the change in Gibbs free energy. These values were between −23.7 and −33.3 kJ mol^{-1}. The examined process was entropy-driven, as the entropic term ($T\Delta S_b$) is higher than the enthalpic one. The obtained values for the change in Gibbs free energy of binding were in the same range as for another copper(II) complex

with (E)-1-(4-(diethylamino)-2-hydroxybenzylidene)-4,4-dimethyl-thiosemicarbazide in reference [66].

Table 4. The Stern–Volmer constant (K_{SV}), binding constant (K_b), Hill coefficient (n), and thermodynamic parameters of $[Cu(PLSC)Cl(H_2O)](NO_3)(H_2O)$ binding to HSA.

Compound	T [K]	Kb [M^{-1}]	R	n	ΔH_b [kJ mol^{-1}]	ΔS_b [J mol^{-1} K^{-1}]	ΔG_b [kJ mol^{-1}]
1	300	1.01×10^{-4}	0.994	0.929	264.1	959.2	−23.7
	305	5.11×10^{-5}	0.997	1.144			−28.5
	310	5.48×10^{-5}	0.991	1.226			−33.3

Molecular docking simulations were performed to examine the binding process at the molecular level. In the structure of 2BXN, myristic acid molecules are originally situated in fatty acid binding sites 1, 2, 3, 4, 5, and 6 (FA1, FA2, FA3, FA4, FA5, FA6). The Cu(II)-complex binds specifically to the fatty acid 8 (FA8) binding site, located adjacent to the Trp214 side chain (Figure 7a). The calculated change in Gibbs free energy of binding (−22.9 kJ mol^{-1}) closely matches the experimentally determined value of −23.7 kJ mol^{-1}. Figure 7 provides detailed insights into the interactions that govern the binding of the Cu-complex to the FA8 site as its preferred binding location.

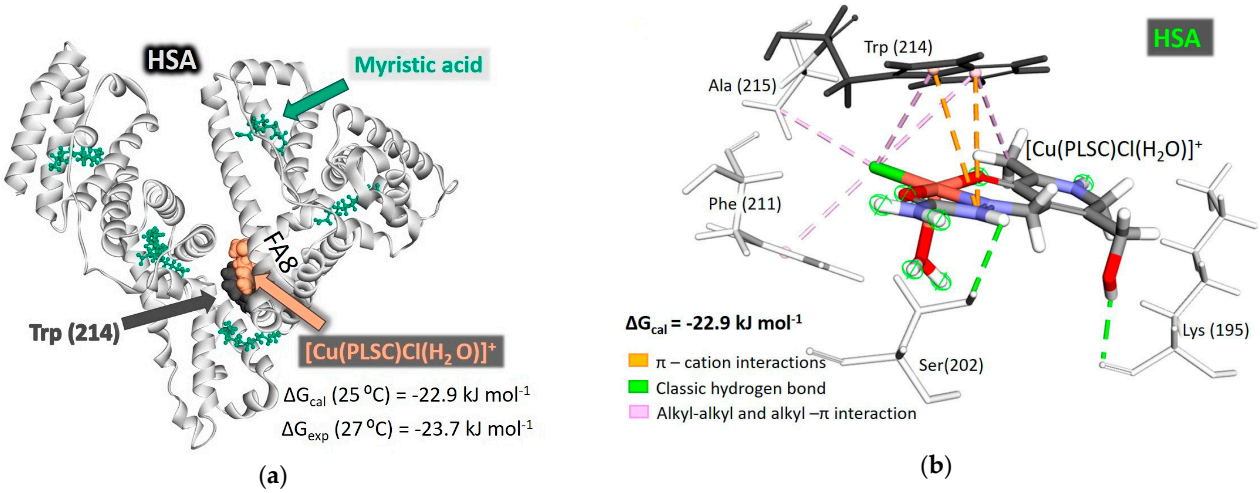


Figure 7. (**a**) The pale gray structure represents HSA, with green ball-and-stick models indicating myristic acid molecules. In the FA8 binding site, dark gray spheres depict Trp214, while orange spheres represent the $[Cu(PLSC)Cl(H_2O)]^+$ complex. The calculated (ΔG_{cal}) and experimentally determined (ΔG_{exp}) binding energies are provided. (**b**) Interactions of the Cu complex within the FA8 binding site of the HSA structure (PDB ID: 2BXN) in 3D representation and the calculated change in Gibbs free energy (ΔG_{cal}).

The Cu(II) complex interactions with surrounding amino acids are depicted in 3D (Figure 7b) representation. The Cu complex establishes direct contact with Trp214, forming most interactions within the FA8 binding site. Notably, the Cu(II) complex is oriented parallel to the aromatic ring of Trp214, engaging in π-π stacking and edge-on interactions, such as π-cation or π-alkyl interactions, depending on the functional groups of the Cu complex involved.

The π-π stacking interactions exhibit an off-centered parallel orientation, described as a "parallel offset arrangement" [67,68], between the aromatic rings of Trp214 and the chelate rings formed by the two oxygen atoms and one nitrogen atom of the PLSC ligand bound to the copper central ion. Specifically, these interactions occur between the five-membered and six-membered chelate rings of the Cu(II) complex and the aromatic rings of Trp214, with centroid-to-centroid distances of 3.923 Å and 3.820 Å, respectively. Additionally, the

centroid-to-centroid distance between the pyridine ring of the Cu complex and the nearest six-membered aromatic ring of Trp214 measures 4.953 Å, meeting the established criteria for π-π stacking interactions, which typically range from 3.0 to 5.5 Å [69].

It has been demonstrated that π-stacking interactions play a significant role in drug distribution, binding, and controlled drug release [70]. The Cu(II) complex establishes the most numerous contacts with Trp214, involving the π-electron cloud of one or both interacting molecules. π-cation interactions are primarily formed between the N-H^+ group of the PLSC ligand and the aromatic rings of Trp214.

The chloride ligand coordinated with the copper(II) central metal ion is the most active group in establishing interactions, forming four distinct contacts: Cl-π edge-on interactions with both Trp214 rings and the benzene ring of Phe211 as well as an interaction with the alkyl group of Ala215 [71]. The $^+$N–H group is the second most active, participating in three interactions, including a classical hydrogen bond with the hydroxyl group oxygen from Ser202. Another hydrogen bond is observed between the carbonyl (C=O) group of Lys195 and the hydroxyl (OH) group of the Cu(II) complex.

An alkyl-π interaction is found between the methyl group of the Cu complex and the six-membered aromatic ring of Trp214. Notably, the aqueous ligand does not interact with the surrounding amino acid residues.

Previously, the Fe [71] and Ni [6] complexes coordinated with PLSC or their derivatives, PLTSC and PLITSC, were studied. The complexes were octahedral, synthesized with either two identical ligands or one of the ligands being PLSC, PLTSC, or PLITSC, along with three smaller ligands, such as water and the SO_4^{2-} ion. Similarly, all the complexes bound near Trp214, causing quenching in spectrofluorimetric experiments. Their binding energies were slightly higher, reaching up to 30 kJ mol^{-1}. However, due to their octahedral structure, the rings formed by the coordination of PLSC, PLTSC, and PLITSC could not approach closely enough or align parallel to the aromatic rings of Trp214 and the surrounding sidechain residues to establish π-π stacking interactions.

4. Conclusions

The compound $[Cu(PLSC)Cl(H_2O)](NO_3)(H_2O)$ was obtained from the mixture of PLSC ligand and copper(II) chloride in the presence of nitric acid. The structure was solved by X-ray crystallography, and it was shown that the compound crystallized in the triclinic P_{-1} space group. The obtained compound contained infinite linear chains in which cations were connected through hydrogen bonds. Two broad peaks at 398 and 298 nm were observed in the UV-VIS spectrum, assigned to the transitions within the PLSC ligand and between the ligand and the central metal ion. The Hirshfeld surface analysis results showed that the most abundant contacts were O···H (32.4%), H···H (28.2%), and Cl···H (9.9%). The crystallographic structure of the neutral species and complex cation were optimized at the B3LYP/6-311++G(d,p)(H,C,N,O)/LanL2DZ(Cu) level of theory. The correlation coefficients and mean absolute errors for comparing experimental and theoretical bond lengths were 0.995 and 0.023 Å for neutral species and 0.996 and 0.025 Å for cationic species. The bond angles were much more prone to the change in the presence of the nitrate anion and co-crystalized solvent molecule, leading to a higher correlation coefficient and lower MAE value in the case of the complex cation than the neutral species. The QTAIM parameters allowed examination of the interactions between the central metal ion and donor atoms and the interactions between the complex cation, nitrate anion, and water molecule. The electrostatic potential map showed the positions of positive and negative potential. The experimental FTIR spectra were assigned based on the theoretical prediction of the optimized structure. The most prominent bands were selected, and their shift in spectrum of complex concerning spectrum of ligand were discussed. The binding constants between the obtained complex and HSA were 1.01×10^{-4}, 5.11×10^{-5}, and 5.48×10^{-5} M^{-1} in the temperature range between 27 and 37 °C. Based on these values, the thermodynamic parameters of binding were determined, and the changes in enthalpy and entropy of the process were 264.1 kJ mol^{-1} and 959.2 J mol^{-1} K^{-1}, respectively. The

changes in Gibbs free energy of binding were −23.7 and −33.3 kJ mol^{-1}. The molecular docking simulations were used for the examination of the binding mechanism, and the most probable position was FA8 in the vicinity of Trp214. The calculated change in Gibbs free energy was −22.9 kJ mol^{-1}, which corresponded well to the experimental value. The changes in the chemical environment of Trp214 led to the experimentally observed decrease in fluorescence emission. Further experimental studies and examinations of the interactions with other biomolecules are advised.

Supplementary Materials: The following supporting information can be downloaded at: https://www.mdpi.com/article/10.3390/cryst14121106/s1, Table S1: Experimental and optimized (at B3LYP/6-311++G(d,p)(H,C,N,O)/LanL2DZ(Cu) level of theory) bond lengths (in Å); Table S2: Experimental and optimized (at B3LYP/6-311++G(d,p)(H,C,N,O)/LanL2DZ(Cu) level of theory) bond angles (in °); Figure S1: UV-VIS spectrum of [Cu(PLSC)Cl(H_2O)](NO_3)(H_2O); Figure S2: The fingerprint plots of the most numerous contacts in the crystallographic structure of [Cu(PLSC)Cl(H_2O)](NO_3)(H_2O).

Author Contributions: Conceptualization, V.J. and D.D.; methodology, A.R., A.A.A. and J.M.Ž.; software, A.R., J.M.Ž., M.A.A. and E.A.A.; validation, O.A.O.A., S.Y.R., A.A.A. and M.A.A.; formal analysis, A.R., J.M.Ž., E.A.A. and O.A.O.A.; investigation, S.Y.R., A.A.A. and M.A.A.; resources, E.A.A., O.A.O.A., S.Y.R. and A.A.A.; data curation, M.A.H., E.A.A. and O.A.O.A.; writing—original draft preparation, S.Y.R., A.R., M.A.H. and J.M.Ž.; writing—review and editing, V.J. and D.D.; visualization, D.D., A.R., M.A.H. and J.M.Ž.; supervision, D.D.; project administration, V.J.; funding acquisition, V.J. All authors have read and agreed to the published version of the manuscript.

Funding: This research was funded by the Scientific Research Deanship at the University of Ha'il, Kingdom of Saudi Arabia, grant number RG-24009.

Data Availability Statement: Data are contained in this article. Further inquiries can be directed to the corresponding author.

Acknowledgments: The authors are thankful to the University of Ha'il, Kingdom of Saudi Arabia. This research was funded by Scientific Research Deanship at University of Ha'il—Saudi Arabia, through project number RG-24009.

Conflicts of Interest: The authors declare no conflicts of interest. The funders had no role in the design of the study; in the collection, analyses, or interpretation of data; in the writing of the manuscript; or in the decision to publish the results.

References

1. Casas, J.S.; García-Tasende, M.S.; Sordo, J. Main group metal complexes of semicarbazones and thiosemicarbazones. A structural review. *Coord. Chem. Rev.* **2000**, *209*, 197–261. [CrossRef]
2. Mustafa, Y.F. Modern Developments in the Application and Function of Metal/Metal Oxide Nanocomposite–Based Antibacterial Agents. *Bionanoscience* **2023**, *13*, 840–852. [CrossRef]
3. Pal, R.; Kumar, V.; Gupta, A.K.; Beniwal, V. Synthesis, characterization and DNA photocleavage study of a novel dehydroacetic acid based hydrazone Schiff's base and its metal complexes. *Med. Chem. Res.* **2014**, *23*, 3327–3335. [CrossRef]
4. Padhyé, S.; Kauffman, G.B. Transition metal complexes of semicarbazones and thiosemicarbazones. *Coord. Chem. Rev.* **1985**, *63*, 127–160. [CrossRef]
5. Alsoliemy, A.; Alrefaei, A.F.; Almehmadi, S.J.; Almehmadi, S.J.; Hossan, A.; Khalifa, M.E.; El-Metwaly, N.M. Synthesis, characterization and self-assembly of new cholesteryl-substitued sym-tetrazine: Fluorescence, gelation and mesogenic properties. *J. Mol. Liq.* **2021**, *342*, 117543. [CrossRef]
6. Jevtovic, V.; Golubović, L.; Alshammari, O.A.O.; Alhar, M.S.; Alanazi, T.Y.A.; Radulović, A.; Nakarada, Đ.; Dimitrić Marković, J.; Rakić, A.; Dimić, D. Structural, Antioxidant, and Protein/DNA-Binding Properties of Sulfate-Coordinated Ni(II) Complex with Pyridoxal-Semicarbazone (PLSC) Ligand. *Inorganics* **2024**, *12*, 280. [CrossRef]
7. Mir, I.A.; Ain, Q.U.; Qadir, T.; Malik, A.Q.; Jan, S.; Shahverdi, S.; Nabi, S.A. A review of semicarbazone-derived metal complexes for application in biomedicine and related fields. *J. Mol. Struct.* **2024**, *1295*, 136216. [CrossRef]
8. Blower, P.J.; Castle, T.C.; Cowley, A.R.; Dilworth, J.R.; Donnelly, P.S.; Labisbal, E.; Sowrey, F.E.; Teat, S.J.; Went, M.J. Structural trends in copper(ii) bis(thiosemicarbazone) radiopharmaceuticals. *Dalton Trans.* **2003**, *23*, 4416–4425. [CrossRef]
9. Muleta, F.; Desalegn, T. Synthesis, In Silico, and Biological Applications of Novel Heteroleptic Copper (II) Complex of Natural Product-Based Semicarbazone Ligands. *J. Chem.* **2022**, *2022*, 497117. [CrossRef]
10. Chau, P.; Teo, G.L.; Li, Y.; Lee, P.P.F.; Yan, Y.K. Synthesis and cytotoxicity of copper(II) semicarbazone complexes with lipophilic counter-anions. *Inorganica Chim. Acta* **2024**, *570*, 122175. [CrossRef]

11. Petrasheuskaya, T.V.; Kovács, F.; Igaz, N.; Rónavári, A.; Hajdu, B.; Bereczki, L.; May, N.V.; Spengler, G.; Gyurcsik, B.; Kiricsi, M.; et al. Estradiol-Based Salicylaldehyde (Thio)Semicarbazones and Their Copper Complexes with Anticancer, Antibacterial and Antioxidant Activities. *Molecules* **2022**, *28*, 54. [CrossRef] [PubMed]
12. Sithambaresan, M.; Kurup, M.R.P.; Serdaroğlu, G.; Kaya, S. Copper(II) chelates derived from an N,N,O-tridentate 2-pyridinecarboxaldehyde-N4-phenylsemicarbazone: Synthesis, spectral aspects, crystal structure, FMO and NBO analysis. *J. Mol. Struct.* **2023**, *1277*, 134866. [CrossRef]
13. Adly, O.M.I.; Taha, A.; Fahmy, S.A. Synthesis, characterization of binary and ternary copper(II)-semicarbazone complexes: Solvatochromic shift, dipole moments and TD-DFT calculations. *J. Mol. Struct.* **2019**, *1186*, 362–376. [CrossRef]
14. Soek, R.N.; da C. Gouveia, T.L.; Garbelini, E.R.; dos R. Crespan, E.; Pineider, F.; Poneti, G.; Machado, G.S.; Ribeiro, R.R.; Hörner, M.; Nunes, F.S. Structural, Magnetic, Spectroscopic and Density Functional Theory (DFT) Analysis of Bis((1-((E)-2-pyridinylmethylidene)semicarbazone)copper(II)sulfate) Dihydrate Complex. *ChemistrySelect* **2017**, *2*, 8451–8458. [CrossRef]
15. Salbego, P.R.S.; Weimer, G.H.; Meyer, A.R.; Soek, R.N.; Garbelini, E.R.; Nunes, F.S.; Zanatta, N.; Bonacorso, H.G.; Hörner, M.; Martins, M.A.P. Formation of a penta- or hexacoordinated Cu–(II) semicarbazone complex: Revisiting semicarbazone metal complexes. *J. Mol. Struct.* **2021**, *1231*, 129942. [CrossRef]
16. Pires, F.C.; Bresolin, L.; Gervini, V.C.; Tirloni, B.; Bof de Oliveira, A. Synthesis, crystal structure and Hirshfeld analysis of a crystalline compound comprising a 1/1 mixture of 1-[(1 R,4 S)- and 1-[(1 S,4 R)-1,7,7-trimethyl-2-oxobicyclo[2.2.1]heptan-3-ylidene]hydrazinecarbothioamide. *Acta Crystallogr. Sect. E Crystallogr. Commun.* **2020**, *76*, 115–120. [CrossRef]
17. Sooraj, M.; Manoj, E.; Prathapachandra Kurup, M.R. Solvothermal self-assembly of a novel metal-organic square grid complex using a biscarbohydrazone ligand building block: Crystal structures, Hirshfeld and void surface analyses, band gap calculations and DFT studies. *Polyhedron* **2023**, *244*, 116583. [CrossRef]
18. Muleta, F.; Desalegn, T.; Demissie, T.B.; Eswaramoorthy, R.; Murthy, H.C.A.; Chan, K.-Y.; Davids, B.L.; Ngwira, K.J. Synthesis, molecular docking, and biological studies of novel heteroleptic Cu(II) and Zn(II) complexes of natural product-based semicarbazone derivatives. *J. Mol. Struct.* **2023**, *1274*, 134405. [CrossRef]
19. Muleta, F.; Desalegn, T.; Eswaramoorthy, R.; Garg, A. Synthesis, characterization, in-silico, and in-vitro biological studies of Cu(II), Zn(II) complexes of semicarbazone, thiosemicarbazone derivatives of dehydrozingerone. *J. Mol. Struct.* **2022**, *1268*, 133632. [CrossRef]
20. Knežević, N.Ž.; Leovac, V.M.; Jevtović, V.S.; Grgurić-Šipka, S.; Sabo, T.J. Platinum(IV) complex with pyridoxal semicarbazone. *Inorg. Chem. Commun.* **2003**, *6*, 561–564. [CrossRef]
21. Cordes, E.H.; Jencks, W.P. Semicarbazone Formation from Pyridoxal, Pyridoxal Phosphate, and Their Schiff Bases. *Biochemistry* **1962**, *1*, 773–778. [CrossRef] [PubMed]
22. Poleti, D.; Karanović, L.; Leovac, V.M.; Jevtović, V.S. Dibromo(pyridoxal semicarbazone-$\kappa^3N^1,O^3,O^{3\prime}$)copper(II). *Acta Crystallogr. Sect. C Cryst. Struct. Commun.* **2003**, *59*, 73–75. [CrossRef]
23. Vojinović-Ješić, L.S.; Rodić, M.V.; Barta Holló, B.; Ivković, S.A.; Leovac, V.M.; Mészáros Szécsényi, K. Synthesis, characterization and thermal behavior of copper(II) complexes with pyridoxal thiosemi (PLTSC)- and S-methylisothiosemicarbazone (PLITSC). *J. Therm. Anal. Calorim.* **2016**, *123*, 2069–2079. [CrossRef]
24. Vidovic, D.; Radulovic, A.; Jevtovic, V. Synthesis, characterization and structural analysis of new copper(II) complexes incorporating a pyridoxal-semicarbazone ligand. *Polyhedron* **2011**, *30*, 16–21. [CrossRef]
25. Al-Zahrani, S.; Jevtovic, V.; Alenezi, K.; El, M.; Haque, A.; Vidovic, D. Electrocatalytic hydrogen evolution upon reduction of pyridoxal semicarbazone and thiosemicarbazone-based Cu(II) complexes. *J. Serbian Chem. Soc.* **2022**, *87*, 345–354. [CrossRef]
26. Vojinović-Ješić, L.S.; Jovanović, L.S.; Leovac, V.M.; Radanović, M.M.; Rodić, M.V.; Barta Holló, B.; Mészásaros Szécsényi, K.; Ivković, S.A. Transition metal complexes with thiosemicarbazide-based ligands. Part 63. Syntheses, structures and physicochemical characterization of the first chromium(III) complexes with pyridoxal semi- and thiosemicarbazones. *Polyhedron* **2015**, *101*, 196–205. [CrossRef]
27. Ivković, S.A.; Vojinović-Ješić, L.S.; Leovac, V.M.; Rodić, M.V.; Novaković, S.B.; Bogdanović, G.A. Transition metal complexes with thiosemicarbazide-based ligands. Part 61. Comparative analysis of structural properties of the pyridoxal thiosemicarbazone ligands. Crystal structure of PLTSC·HCl·2H2O and its complex [Fe(PLTSC)Cl2(H2O)]Cl. *Struct. Chem.* **2015**, *26*, 269–277. [CrossRef]
28. Oxford Diffraction/Agilent Technologies UK Ltd. *CrysAlisPRO*; Oxford Diffraction/Agilent Technologies UK Ltd.: Yarnton, UK, 2017; Volume 717.
29. Sheldrick, G.M. *SHELXT*—Integrated space-group and crystal-structure determination. *Acta Crystallogr. Sect. A Found. Adv.* **2015**, *71*, 3–8. [CrossRef]
30. Dolomanov, O.V.; Bourhis, L.J.; Gildea, R.J.; Howard, J.A.K.; Puschmann, H. OLEX2: A complete structure solution, refinement and analysis program. *J. Appl. Crystallogr.* **2009**, *42*, 339–341. [CrossRef]
31. Turner, M.J.; McKinnon, J.J.; Wolff, S.K.; Grimwood, D.J.; Spackman, P.R.; Jayatilaka, D.; Spackman, M.A. *CrystalExplorer17*; University of Western Australia: Perth, Australia, 2017.
32. Spackman, M.A.; Jayatilaka, D. Hirshfeld surface analysis. *CrystEngComm* **2009**, *11*, 19–32. [CrossRef]
33. Grabowsky, S.; Dean, P.M.; Skelton, B.W.; Sobolev, A.N.; Spackman, M.A.; White, A.H. Crystal packing in the 2-R,4-oxo-[1,3-a/b]-naphthodioxanes—Hirshfeld surface analysis and melting point correlation. *CrystEngComm* **2012**, *14*, 1083–1093. [CrossRef]

34. Frisch, M.J.; Trucks, G.W.; Schlegel, H.B.; Scuseria, G.E.; Robb, M.A.; Cheeseman, J.R.; Scalmani, G.; Barone, V.; Mennucci, B.; Petersson, G.A.; et al. *Gaussian 09, Revision C.01*; Gaussian, Inc.: Wallingford, CT, USA, 2009.
35. Becke, A.D. Density-functional thermochemistry. III. The role of exact exchange. *J. Chem. Phys.* **1993**, *98*, 5648–5652. [CrossRef]
36. Dunning, T.H. Gaussian basis sets for use in correlated molecular calculations. I. The atoms boron through neon and hydrogen. *J. Chem. Phys.* **1989**, *90*, 1007. [CrossRef]
37. Hay, P.J.; Wadt, W.R. Ab initio effective core potentials for molecular calculations. Potentials for K to Au including the outermost core orbitale. *J. Chem. Phys.* **1985**, *82*, 299–310. [CrossRef]
38. Hay, P.J.; Wadt, W.R. Ab initio effective core potentials for molecular calculations. Potentials for the transition metal atoms Sc to Hg. *J. Chem. Phys.* **1985**, *82*, 270–283. [CrossRef]
39. Bader, R.F.W. Atoms in molecules. *Acc. Chem. Res.* **1985**, *18*, 9–15. [CrossRef]
40. Bader, R.F.W. *Atoms in Molecules: A Quantum Theory*; Oxford University Press: Oxford, UK, 1990.
41. Todd, A. *AIMAll; Version 19.10.12*; Keith, T.K., Ed.; Gristmill Software: Overland Park, KS, USA, 2019.
42. Bader, R.F.W.; Carroll, M.T.; Cheeseman, J.R.; Chang, C. Properties of atoms in molecules: Atomic volumes. *J. Am. Chem. Soc.* **1987**, *109*, 7968–7979. [CrossRef]
43. Wu, D.; Liu, D.; Zhang, Y.; Zhang, Z.; Li, H. Unravelling the binding mechanism of benproperine with human serum albumin: A docking, fluorometric, and thermodynamic approach. *Eur. J. Med. Chem.* **2018**, *146*, 245–250. [CrossRef]
44. Ghuman, J.; Zunszain, P.A.; Petitpas, I.; Bhattacharya, A.A.; Otagiri, M.; Curry, S. Structural Basis of the Drug-binding Specificity of Human Serum Albumin. *J. Mol. Biol.* **2005**, *353*, 38–52. [CrossRef]
45. Valdés-Tresanco, M.S.; Valdés-Tresanco, M.E.; Valiente, P.A.; Moreno, E. AMDock: A versatile graphical tool for assisting molecular docking with Autodock Vina and Autodock4. *Biol. Direct* **2020**, *15*, 12. [CrossRef]
46. Leovac, V.M.; Jovanović, L.S.; Divjaković, V.; Pevec, A.; Leban, I.; Armbruster, T. Transition metal complexes with thiosemicarbazide-based ligands. Part LIV. Nickel(II) complexes with pyridoxal semi- (PLSC) and thiosemicarbazone (PLTSC). Crystal and molecular structure of $[Ni(PLSC)(H_2O)_3](NO_3)_2$ and $[Ni(PLTSC\text{-}H)py]NO_3$. *Polyhedron* **2007**, *26*, 49–58. [CrossRef]
47. Beraldo, H.; Nacif, W.F.; Teixeira, L.R.; Rebouças, J.S. Cobalt(II) and nickel(II) complexes of N(4′) substituted 3- and 4-acetylpyridine thiosemicarbazones. *Transit. Met. Chem.* **2002**, *27*, 85–88. [CrossRef]
48. West, D.X.; Billeh, I.S.; Jasinski, J.P.; Jasinski, J.M.; Butcher, R.J. Complexes of N(4)-cyclohexylsemicarbazones and N(4)-cyclohexylthiosemicarbazones derived from 2-formyl-, 2-acetyl- and 2-benzoylpyridine. *Transit. Met. Chem.* **1998**, *23*, 209–214. [CrossRef]
49. Geary, W.J. The use of conductivity measurements in organic solvents for the characterisation of coordination compounds. *Coord. Chem. Rev.* **1971**, *7*, 81–122. [CrossRef]
50. Andrić, J.M.; Janjić, G.V.; Ninković, D.B.; Zarić, S.D. The influence of water molecule coordination to a metal ion on water hydrogen bonds. *Phys. Chem. Chem. Phys.* **2012**, *14*, 10896. [CrossRef]
51. Živković, J.M.; Milovanović, M.R.; Zarić, S.D. Hydrogen Bonds of Coordinated Ethylenediamine and a Water Molecule: Joint Crystallographic and Computational Study of Second Coordination Sphere. *Cryst. Growth Des.* **2022**, *22*, 5198–5205. [CrossRef]
52. Hueso-Ureña, F.; Jiménez-Pulido, S.B.; Fernández-Liencres, M.P.; Fernández-Gómez, M.; Moreno-Carretero, M.N. A new five-coordinated CuIP2NO2 system: XRD structure of 6-acetyl-1,3,7-trimethyl-pteridine-2,4(1H,3H)-dione and its Cu(i) (N5,O61,O4)-tridentate complex with triphenylphosphine. An AIM study of the nature of metal–ligand bonds. *Dalt. Trans.* **2008**, *45*, 6461–6466. [CrossRef]
53. Fabijanić, I.; Matković-Čalogović, D.; Pilepić, V.; Ivanišević, I.; Mohaček-Grošev, V.; Sanković, K. New investigations of the guanine trichloro cuprate(II) complex crystal. *J. Mol. Struct.* **2017**, *1128*, 317–324. [CrossRef]
54. Kasalović, M.P.; Jelača, S.; Milanović, Ž.; Maksimović-Ivanić, D.; Mijatović, S.; Lađarević, J.; Božić, B.; Marković, Z.; Dunđerović, D.; Rüffer, T.; et al. Novel triphenyltin(iv) compounds with carboxylato *N* -functionalized 2-quinolones as promising potential anticancer drug candidates: In vitro and in vivo evaluation. *Dalt. Trans.* **2024**, *53*, 8298–8314. [CrossRef]
55. Soliman, S.M.; Albering, J.; Abu-Youssef, M.A.M. Structural analyses of two new highly distorted octahedral copper(II) complexes with quinoline-type ligands; Hirshfeld, AIM and NBO studies. *Polyhedron* **2017**, *127*, 36–50. [CrossRef]
56. Lepetit, C.; Vabre, B.; Canac, Y.; Alikhani, M.E.; Zargarian, D. Pentacoordinated, square pyramidal cationic PCP Ni(II) pincer complexes: ELF and QTAIM topological analyses of nickel–triflate interactions. *Theor. Chem. Acc.* **2018**, *137*, 141. [CrossRef]
57. Bianchi, R.; Gervasio, G.; Marabello, D. Experimental Electron Density Analysis of $Mn_2(CO)_{10}$: Metal—Metal and Metal—Ligand Bond Characterization. *Inorg. Chem.* **2000**, *39*, 2360–2366. [CrossRef]
58. Espinosa, E.; Molins, E.; Lecomte, C. Hydrogen bond strengths revealed by topological analyses of experimentally observed electron densities. *Chem. Phys. Lett.* **1998**, *285*, 170–173. [CrossRef]
59. Dennington, R.; Todd, K.; Millam, J. *GausView 6*; Semichem Inc.: Shawnee Mission, KS, USA, 2016.
60. Osman, U.M.; Silvarajoo, S.; Kamarudin, K.H.; Tahir, M.I.M.; Kwong, H.C. Ni(II) complex containing a thiosemicarbazone ligand: Synthesis, spectroscopy, single-crystal X-ray crystallographic and conductivity studies. *J. Mol. Struct.* **2021**, *1223*, 128994. [CrossRef]
61. Devi, J.; Yadav, M.; Jindal, D.K.; Kumar, D.; Poornachandra, Y. Synthesis, spectroscopic characterization, biological screening and in vitro cytotoxic studies of 4-methyl-3-thiosemicarbazone derived Schiff bases and their Co (II), Ni (II), Cu (II) and Zn (II) complexes. *Appl. Organomet. Chem.* **2019**, *33*, e5154. [CrossRef]

62. Ferrari Belicchi, M.; Fava Gasparri, G.; Leporati, E.; Pelizzi, C.; Tarasconi, P.; Tosi, G. Structure of Pyridoxa I Th iosem icar bazone Tr i hyd rate and Spectroscopic Properties of its Metal Complexes t. *J. Chem. Soc. Dalt. Trans.* **1986**, *3*, 1–6.
63. Bishop, J.L.; King, S.J.; Lane, M.D.; Brown, A.J.; Lafuente, B.; Hiroi, T.; Roberts, R.; Swayze, G.A.; Lin, J.-F.; Sánchez Román, M. Spectral Properties of Anhydrous Carbonates and Nitrates. *Earth Space Sci.* **2021**, *8*, e2021EA001844. [CrossRef]
64. Jevtovic, V.; Alshammari, N.; Latif, S.; Alsukaibi, A.K.D.; Humaidi, J.; Alanazi, T.Y.A.; Abdulaziz, F.; Matalka, S.I.; Pantelić, N.Đ.; Marković, M.; et al. Synthesis, Crystal Structure, Theoretical Calculations, Antibacterial Activity, Electrochemical Behavior, and Molecular Docking of Ni(II) and Cu(II) Complexes with Pyridoxal-Semicarbazone. *Molecules* **2022**, *27*, 6322. [CrossRef]
65. Sun, J.; Huang, Y.; Zheng, C.; Zhou, Y.; Liu, Y.; Liu, J. Ruthenium (II) Complexes Interact with Human Serum Albumin and Induce Apoptosis of Tumor Cells. *Biol. Trace Elem. Res.* **2015**, *163*, 266–274. [CrossRef]
66. Ganorkar, K.; Mukherjee, S.; Singh, P.; Ghosh, S.K. Stabilization of a potential anticancer thiosemicarbazone derivative in Sudlow site I of human serum albumin: In vitro spectroscopy coupled with molecular dynamics simulation. *Biophys. Chem.* **2021**, *269*, 106509. [CrossRef]
67. McGaughey, G.B.; Gagné, M.; Rappé, A.K. π-Stacking interactions. Alive and well in proteins. *J. Biol. Chem.* **1998**, *273*, 15458–15463. [CrossRef] [PubMed]
68. Martinez, C.R.; Iverson, B.L. Rethinking the term "pi-stacking". *Chem. Sci.* **2012**, *3*, 2191. [CrossRef]
69. Choudhury, R.R.; Chitra, R. Stacking interaction between homostacks of simple aromatics and the factors influencing these interactions. *CrystEngComm* **2010**, *12*, 2113. [CrossRef]
70. Zhuang, W.-R.; Wang, Y.; Cui, P.-F.; Xing, L.; Lee, J.; Kim, D.; Jiang, H.-L.; Oh, Y.-K. Applications of π-π stacking interactions in the design of drug-delivery systems. *J. Control. Release* **2019**, *294*, 311–326. [CrossRef] [PubMed]
71. Jevtovic, V.; Golubović, L.; Alshammari, B.; Alshammari, M.R.; Rajeh, S.Y.; Alreshidi, M.A.; Alshammari, O.A.O.; Rakić, A.; Dimić, D. Crystal Structure, Theoretical Analysis, and Protein/DNA Binding Activity of Iron(III) Complex Containing Differently Protonated Pyridoxal–S-Methyl-Isothiosemicarbazone Ligands. *Int. J. Mol. Sci.* **2024**, *25*, 7058. [CrossRef]

Disclaimer/Publisher's Note: The statements, opinions and data contained in all publications are solely those of the individual author(s) and contributor(s) and not of MDPI and/or the editor(s). MDPI and/or the editor(s) disclaim responsibility for any injury to people or property resulting from any ideas, methods, instructions or products referred to in the content.